Thermoelectric Properties of Antimony Selenide Hexagonal Nanotubes

Jose A. Hernandez^{1,2}, Luis F. Fonseca^{1*}, Michael T. Pettes³, Miguel Jose-Yacaman⁴

- ¹ Department of Physics University of Puerto Rico Rio Piedras Campus, San Juan PR 00931, USA.
- ² Molecular Science Research Center University of Puerto Rico, San Juan PR 00926, USA.
- ³ Center for Integrated Nanotechnologies (CINT), Materials Physics and Applications Division, Los Alamos National Laboratory, Los Alamos, New Mexico, 87545, USA.
- ⁴ Department of Applied Physics and Materials Science, Northern Arizona University, Flagstaff, AZ 86011

E-mail: luis.fonseca@upr.edu

Received xxxxxx Accepted for publication xxxxxx Published xxxxxx

Abstract

Antimony Selenide (Sb₂Se₃) is a material widely used in photodetectors and relatively new as possible material for thermoelectric applications. Taking advantage of the new properties after nanoscale fabrication, this material shows great potential for the development of efficient low temperature thermoelectric devices. Here we study the synthesis, the crystal properties and the thermal and thermoelectric transport response of Sb₂Se₃ hexagonal nanotubes (HNT) in the temperature range between 120K and 370K. HNT have a moderate electrical conductivity $\sim\!10^2 \text{Sm}^{-1}$ while maintaining a reasonable Seebeck coefficient ~ 430 μVK^{-1} at 370K. The electrical conductivity in Sb₂Se₃ HNT is about 5 orders of magnitude larger and its thermal conductivity one half of what is found in bulk. Moreover, the calculated figure of merit (ZT) at room temperature is the largest value reported in antimony selenide 1D structures.

Keywords: Thermoelectric, Nanotube, Antimony Selenide, Sb₂Se₃

1. Introduction

Antimony Selenide Sb_2Se_3 is a semiconductor with a direct band gap around 1.0-1.2 eV and orthorhombic layered crystal structure. The electrical and optical properties of this material have attracted great attention in recent years for a variety of applications including switching, [1-3] photovoltaics, [4-9] ion batteries, [10] and thermoelectricity. [11-14] Sb_2Se_3 nanostructures have been grown in different ways: gas induced reduction, solvo- and hydro-thermal routes, chemical vapor deposition (CVD), pulsed laser deposition (PLD) and others. [4,5, 15-18] Its applicability in thermoelectricity starts with a high Seebeck coefficient (S) and relatively low thermal conductivity (κ). Its thermoelectric power factor however becomes reduced due to its low dark electrical conductivity (σ).

In recent years, successful syntheses of Sb₂Se₃ 1-D structures have been demonstrated using different synthesis approaches. Reports about 1-D Sb₂Se₃ nanostructures have emphasized on the synthesis, [15, 19-21] the photo-response, [5, 8, 9, or the electrochemical response. [10] In most cases, the preferential growth is along the [001] crystal direction (c-axis) but [010] growth has also been reported. [13,22] Nanowires (NWs) with relatively low dark electrical conductivity have been obtained[2,4,23,24] but with intentional doping, the electrical conductivity has been increased up to 10 orders of magnitude in NWs without a severe reduction in S.[25] At the same time, the growth of the material at the nanoscale increases the surface-to-volume ratio and may take advantage of the scattering of phonons at the surface boundaries to reduce the thermal conductivity, thus possibly bringing increasing energy conversion efficiency. Currently the

maximum measured energy conversion efficiency in thermoelectric materials is around 10% while calculations predict up to 30% in tin selenide nanotubes.^[26]

Multifaceted Sb₂Se₃ nanotube growth has been found in few cases. Using microwave activated solvothermal synthesis, sulfurized nanotubes with high electrical conductivity (3-4 orders of magnitude) were synthesized giving a role to sulfur for the nanorod-to-nanotube conversion. [25] CVD synthesis has been less used for these nanostructures but recently, nanotubes with triangular cross sections have been grown using mica substrates. It was argued that the widely used solvo- and hydro-thermal routes involve organometallic sources and additional reductants and surfactants while CVD only involves pure Se and Sb precursors, thus reducing possible formation of defects, doping and surface adsorptions. The report assigns an important role to the mica substrate versus SiO₂/Si substrate for the successful formation of the nanotubes.

Here, Sb₂Se₃ hexagonal nanotubes (HNT) synthesized by CVD on SiO₂/Si wafers covered with Au were successfully grown along the [010] crystal direction without any intentional dopant. As in previous works reporting nanotube

nanostructure is explained in detail and its electrical and thermoelectrical properties measured as a function of temperature between 100 and 400K by using specialized suspended micro-thermometer devices to simultaneously measure S, σ and κ in single HNTs with a four-points configuration as shown in figure S1 (Supplementary Information). The results confirm p-type electrical transport with a promisingly high electrical conductivity and Seebeck coefficient and reduced thermal conductivity.

2. Experimental Results and Discussion

Sb₂Se₃ HNT were synthesized by CVD technique via vapor liquid solid (VLS) process in a 12-in. horizontal furnace equipped with a 2 in diameter quartz tube. The synthesis was made at atmospheric pressure using a flow of high purity 100 sccm Ar as the gas carrier and Sb (Alpha Aesar 99.998%) and Se (Alpha Aesar 99.998%) powders as precursors. The temperature was set to 550 °C in the precursor zone and many silicon substrates coatined with a 1-3 nm-thick Au film were placed 5 - 15 cm downstream from the hot zone. After 5 hours the system was cooled down naturally, keeping the Ar flow

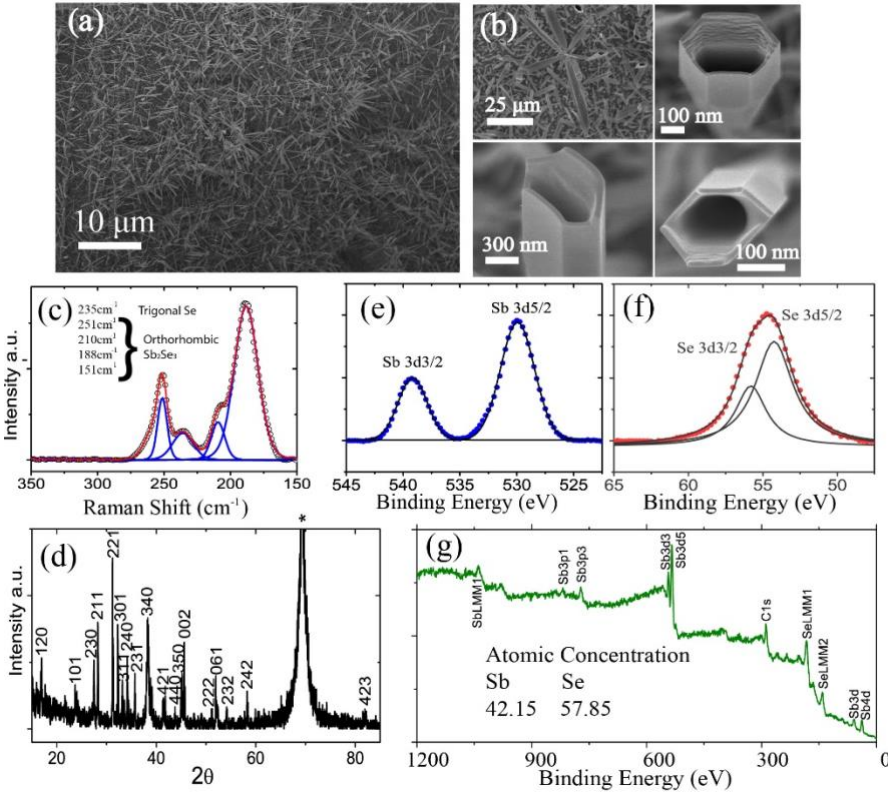


Figure 1: (a,b) SEM image of Sb₂Se₃ hexagonal nanotubes on the substrate. (c) Raman bands of as grown HNT. (d) XRD pattern of as grown material on the substrate. XPS spectra for (e) Sb-3d band, (f) Se-3d band and (g) XPS survey on Si substrate.

growth, the diameters of the structures are larger than what is typically found for nanorods, but the thickness of the walls are below 60nm. The synthesis and characterization of this novel constant. Sb₂Se₃ HNTs grew vertically in large areas as shown in SEM images in figures 1(a,b). Figure 1(b) shows cross sectional areas of as-grown Sb₂Se₃ HNT where the hexagonal

shape is observed; a HNT with an elongated cross section approaching a more rectangular shape is also shown. Rectangular cross sections were reported in ref [25].

The Raman spectrum is shown in figure 1(c) where deconvoluted peaks corresponding to Raman shifts of 251, 210, 188 cm⁻¹ related to the orthorhombic Sb₂Se₃ are confirmed. A peak at 235 cm⁻¹ related to Trigonal Se is possibly formed on Si substrate during the HNT growth. The relatively high intensity of the 251 cm⁻¹ peak compared with the peak at 188 cm⁻¹ exposes the nanoscale nature of the sample, as explained by Farfan et al. [20, 22] The XRD pattern in figure 1(d) confirms that Sb₂Se₃ HNT has an orthorhombic crystal structure and shows all the indexed peaks of Sb₂Se₃ (JCPDS 890821) with a = 11.401, b = 11.943 and c = 3.972 Å. These values were consistent with selected area electron diffraction (SAED) data and HR-TEM crystal planes patterns (figure 2(d)) of the measured Sb₂Se₃ HNT sample (650 nm in diameter). X-ray photoelectron spectroscopy measurements were carried out to study the composition state of the as-grown samples. Figures 1(e) and 1(f) show bands corresponding to Sb 3d and Se 3d binding energies. No obvious contributions from other elements were observed in the survey scan figure 1(g).

Two HNT with 650 and 350 nm in external diameter and

electrical contacts between the HNT and the Pt measuring electrodes were improved by depositing Pt at the sample-electrode contact zones using a Focused Ion Beam (FIB). Figure 2(f) shows SEM-EDS elemental mappings of the sample clarifying its elemental composition. EDS approximated quantification signal (figure 2 (c)) is consistent with the Sb:Se 2:3 stoichiometric ratio and correlated with the XPS results in figure 1(g) to within the accuracy of analytical EDS.

The measured Seebeck coefficient as a function of temperature is displayed in figure 3(a) for the two analyzed samples. In both cases S is positive, revealing that the Sb_2Se_3 HNT have p-type electrical response. S values increase with increasing temperature and are consistent with previous reports for this material. [13, 14, 23, 25, 29] n-type behavior in Sb_2Se_3 crystals is associated with intentional doping. [13, 25] Figure 3(a) includes calculated S values as reported by Rahnamaye Aliabad et. al. [30] for a hole-concentration in the order of 1×10^{19} cm⁻³ for comparison and consistent with Jayaraman et. al. 31

Figure 3(b) shows the variations in σ depending on temperature. The measured electrical conductivity in Sb₂Se₃ HNT is ~5-orders of magnitude larger than Sb₂Se₃ bulk values¹¹ and ~4-orders larger than the reported ones in tubular single crystals¹⁹. Recently Ko et. al [23] synthesized high and low electrical conductivity Sb₂Se₃ NWs with conductivities of

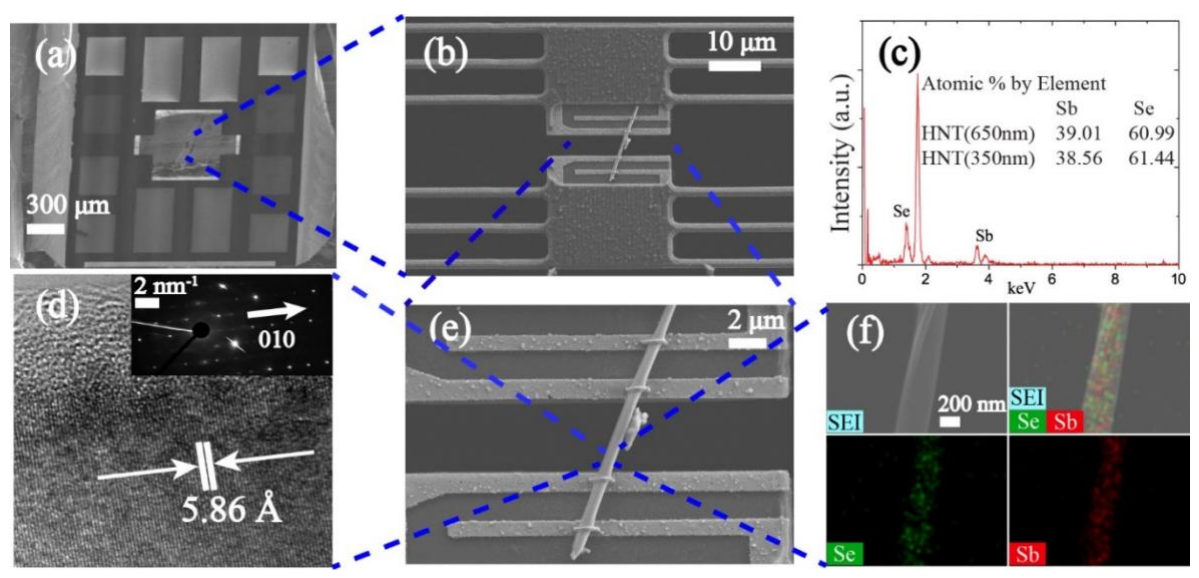


Figure 2: (a,b,e) SEM images of the HNT (650nm in diameter) on a specialized suspended micro-thermometer device at different magnifications. (d) HRTEM image, insert: SAED. (c,f) SEM-EDS mapping and summary of Sb and Se signals of the HNT measured samples.

approximated wall thicknesses between 50 and 60 nm were selected and removed directly from the substrate by micromanipulation and aligned onto the thermoelectric properties measuring micro-device as shown in figure 2. This specialized suspended micro-thermometer device has been proved successful in recent works to determine S, σ and κ parameters of individual 1-D nanostructures. [27,28] The

 \sim 3×10⁴ S/m and 4.3×10⁻⁴ S/m, respectively, showing a strong coupling between the electrical properties, the shape, the crystal structure and the growth conditions of the material. Interpolation of the calculated Seebeck coefficient versus Fermi Energy in reference [31] gives Fermi energy values of \sim 0.034eV and \sim 0.045eV above the valence band edge at 300K for the 350nm HNT and the 650nm HNT, respectively. These

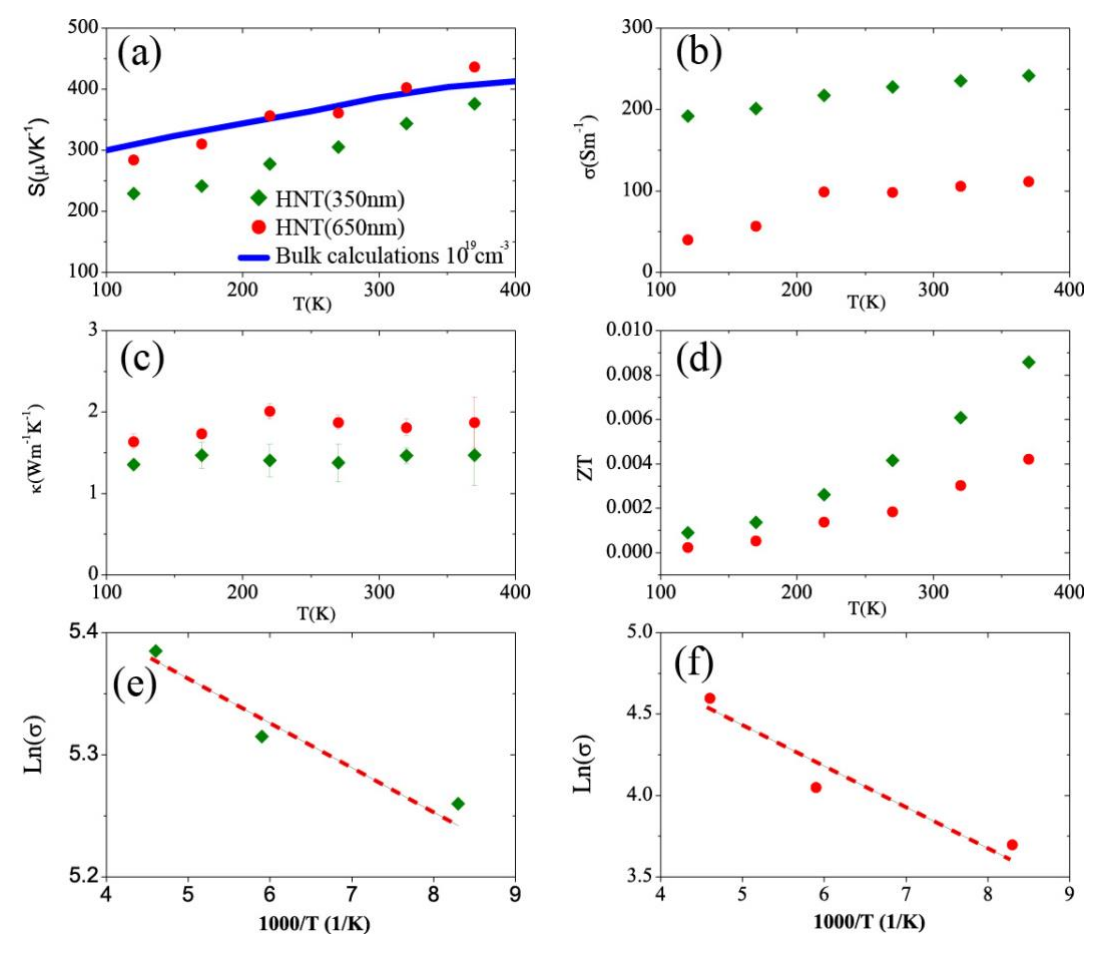


Figure 3: (a) Measured Seebeck coefficient for the two samples as compared with bulk calculations $^{30]}$ (b) Electrical conductivity of the measured samples. (c) Total thermal conductivity κ of the HNT with the error bars. (d) Calculated figure of merit ZT for the samples as a function of temperature. Low temperature linear fittings for ln(s) versus 1000/T for the determination of approximate activation energies for the 350nm nanotube (e) and the 650nm nanotube (f), respectively.

values give density of carriers of the order of $\sim 1.5 \times 10^{19} \text{cm}^{-3}$ and $\sim 0.65 \times 10^{19} \text{cm}^{-3}$, respectively. This degenerate condition is attributed to defects formation during growth and unintentional doping.

The Sb_2Se_3 measurements here reported are in the same order of magnitude of some reported whiskers, 13 and \sim one order of magnitude larger than those obtained in some thin films. $^{[32]}$ Mehta et al. $^{[25]}$ found high electrical conductivity in sulfurized- Sb_2Se_3 nanowires ($\sim 3\times 10^4$ S/m) and nanotubes (3.5×10^2 S/m), lying in the same order of magnitude than the HNTs. $^{[25]}$

The temperature dependences of the thermoelectric parameters are shown in figures 3(a-d). Measured σ in Sb₂Se₃ HNT is thermally activated as shown in figure 3(b). Figures 3(e) and 3(f) show the linear fittings for ln(s) versus 1000/T between 120K and 220K for both samples: (e) 350nm and (f) 650nm. Approximate activation energies obtained from the fittings are: 2.7meV and 19.3meV, respectively. As mentioned

above, the synthesis method used avoids intentional doping and the observed Seebeck coefficient confirms p-type doping. According to experimental observations and modeling, in such conditions, shallow acceptor SeSb antisite defects can be expected. [33] This conclusion is consistent with EDS elemental data in figure 2(g) that favors slight Se-rich condition. The activation energies here obtained are significantly lower than the calculations for such defect and is attributed to the degenerate characteristics of our samples as suggested from the observed S values. The electrical transport of the HNT is then assigned to shallow acceptors states near the valence hand

Figure 3(c) shows the temperature dependence of the thermal conductivity (κ) for all samples. The thermal conductivity remains practically constant with a slight tendency to increase with temperature, and with values between 1.3 to 1.8 Wm⁻¹k⁻¹. These values are half of the ones reported in bulk samples^[34] and of the same order of magnitude than those reported in nanowires and nanotubes. ^[23, 123]

^{25]} The lattice contribution to the thermal conductivity was calculated using the approximation: $\kappa_L = \kappa_{Total} - \sigma LT$. A conservative Lorenz number L was used from the approximation: L=(1.5 +exp(-|S|/116)) ×10⁻⁸ WΩK⁻² [35] that brings values between 1.64–1.52 ×10⁻⁸ WΩK⁻² for the investigated temperature range. Figure 4 confirms that the main contribution to the observed thermal conductivity comes from lattice vibrations in the HNT samples, with boundary scattering dominating transport.

Finally, the thermoelectric figure of merit ZT (ZT = $S^2\sigma/\kappa$) was calculated and shown in figure 3(d). The ZT values have

response with high electrical conductivity attributed to shallow acceptor defects possibly related to a Se-rich condition.

The electrical conductivity of these structures is five orders of magnitude larger than reported bulk values, four orders of magnitude larger than bulk tubular samples, and in the same order of magnitude than what is observed in sulfurized Sb_2Se_3 nanotubes. The thermal conductivity is dominated by phonon transport and reduced to one half of the bulk value, likely due to enhanced surface scattering in the nanostructure boundaries.

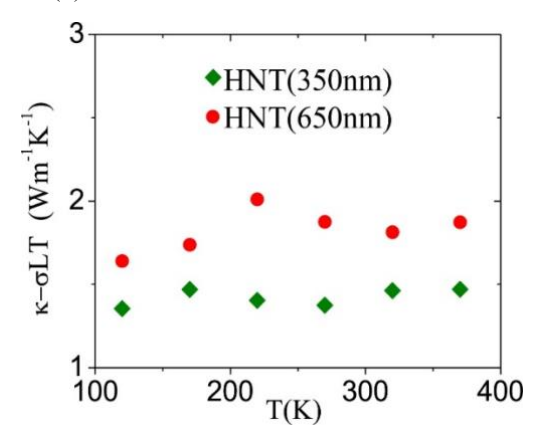


Figure 4: Calculated lattice thermal conductivity as a function

a maximum of ~ 0.0071 at 370K, 4-orders of magnitude larger than reported bulk values.

In all the samples ZT increases with temperature. These results show that Sb₂Se₃ HNTs considerably improve the figure of merit due to the combination of an increasing electrical conductivity and a thermal conductivity that is reduced to a half. This result makes such morphology a preferred one for this material in future hybrid photothermoelectric room temperature applications.

3. Summary

Sb₂Se₃ were synthesized in high yields by CVD with no intentional doping on gold-decorated SiO₂/Si wafers by VLS process from pure Sb and Se precursors. Under the experimental conditions, hexagonal nanotubes were obtained with external diameters above 300nm and with wall thickness in the order of 60nm. The nanotubes show preferential growth along [010] crystal direction. Single HNT were integrated to specialized suspended four-probe microdevices for the direct measurement of electrical and thermal conductances, and Seebeck coefficient, at different temperatures between 120K and 370K in high vacuum. From the electron microscopy characterization, and the thermoelectrical voltage and electrical conductance measurements, the nanostructures show high crystalline quality, purity, and p-type transport

The thermoelectric figure of merit is then enhanced in HNTs and increases four orders of magnitude of what is obtained in bulk samples, making these structures promising ones for room temperature thermoelectrical applications. As far as we know, these ZT values are the largest reported in Sb₂Se₃ 1D nanostructures.

4. Experimental Details

The crystal structure, morphology and chemical composition of as-synthesized samples were characterized by x-ray diffraction - XRD (Rigaku, Cu-Kα radiation with λ =1.5406 Å) and scanning electron microscopy - SEM (JEOL 7500F) and SEM (Hitachi 5500) equipped with an energy dispersive X-ray spectrometer (EDS) (see figure 2(c)) and 2(f)). High resolution electron microscopy and XPS information were obtained with Atomic Resolution Transmission Electron Microscope JEOL ARM 200F and XPS PHI 5600, respectively. The lattice parameters were calculated by calibrating peak positions obtained from XRD and HRTEM-SAED data. The Sb2Se3 HNT were selected directly from the substrate and integrated into a the microdevices by micromanipulation with a tungsten nanotip attached to a Narishige micromanipulator, using a high magnification optical microscope (Nikon eclipse E600). The HNT were attached to the tip by van der Waals forces and moved to the device and aligned properly to let the sample to get into contact with the four Pt electrodes. Once the sample was in place, the argon beam of a JEOL JEM 9310 FIB was used to remove possible contaminants from the surface of the sample at to deposit Pt at the contact sites (see figure 2(e) and figure S2 in Supplementary Information). Each measuring device with the integrated sample was wired by wire bonding (Kulicke & Soffa 4524) to a chip carrier in order to connect them to the measuring setup.

Acknowledgements

L.F.F. NSF Grant HRF-1736093. M.J-Y. The Welch Foundation grant #AX-1615. This work was performed, in part, under user Grant No. 2018BU0032 at the Center for Integrated Nanotechnologies, an Office of Science User Facility operated for the U.S. Department of Energy (DOE) Office of Science. Los Alamos National Laboratory, an affirmative action equal opportunity employer, is managed by Triad National Security, LLC for the U.S. Department of Energy's NNSA, under contract 89233218CNA000001.

References

- [1] N. Platakis , H. Gatos, Phys. Status Solidi (a) 13, K1-K4 (1972).
- [2] S-W. Jung, S-M. Yoon, I-K. You, B-G. Yu, K-W. Koo, J. of Nanosci. Nanotechnol. 11, 1569 (2011).
- [3] C. Liu, Y. Yuan, L. Cheng, J. Su, X. Zhang, X. Li, H. Zhang, M. Xu, J. Li, Results Phys. 13,102228 (2019).
- [4] T. Zhai, M. Ye, L. Li L, X. Fang, M. Liao, Y. Li, Y. Koide, Y. Bando, D. Golberg, Adv. Mater. 22, 4530 (2010).
- [5] D. Choi, Y. Jang, J. Lee, GH. Jeong, D. Whang, SW. Hwang, Sci. Rep. 4, 6714 (2014).
- [6] X. Liu, J. Chen, M. Luo, M. Leng, Z. Xia, Y. Zhou, S. Quin, D. Xue, L. Lv, H. Huand, ACS Appl. Mater. Interfaces. 6,10687 (2014).
- [7] Y. Zhou, L. Wang, S. Chen, S. Qin, X. Liu, J. Chen, D.-J. Xue, M. Luo, Y. Cao, Y. Cheng, E. H. Sargent, J. Tang, Nat. Photonics. 9, 409 (2015).
- [8] Z. Li, X. Liang, G. Li, H. Liu, H. Zhang, J. Guo, J. Chen, K. Shen, X. San, W. Yu, Nat. Commun. 10, 125 (2019).
- [9] Z. Ma, S. Chai, Q. Feng, L. Li, X. Li, L. Huang, D. Liu, J. Sun, R. Jiang, T. Zhai, Small. 15, 1805307 (2019).
- [10] W. Luo, A. Calas, C. Tang, F. Li, L. Zhou, L. Mai, ACS Appl. Mater. Interfaces 8, 35219 (2016).
- [11] J. Black, E. Conwell, S. Seigle, C. Spencer, J. of Phys. Chem. Solids. 2, 240 (1957).
- [12] L. Gribnyak, T. Ivanova, Inorg. Mater. (Engl Transl); (United States). 23, 540 (1987).
- [13] H-J. Wu, P-C. Lee, F-Y. Chiu, S-W. Chen, Y-Y. Chen, J. Mater. Chem. C. 3, 10488 (2015).
- [14] K. W. Sun, T-Y. Ko, M. Shellaiah, Appl. Phys. A. 124, 317 (2018).

- [15] J. Ma, Y. Wang, Y. Wang, Q. Chen, J. Lian, W. Zheng, J. Phys. Chem. C. 113, 13588 (2009).
- [16] J. Ota, SK. Srivastava, Opt. Mater. 32, 1488 (2010).
- [17] T. Zhai, L. Li, X. Wang, X. Fang, Y. Bando, D. Golberg, Adv. Funct. Mater. 20, 4233 (2010).
- [18] J. Ma, Y. Wang, Y. Wang, P. Peng, J. Lian, X. Duan, Z. Liu, X. Liu, Q. Chen, T. Kim, CrystEngComm. 13, 2369 (2011).
- [19] X. Zheng, Y. Xie, L. Zhu, X. Jiang, Y. Jia, W. Song, Y. Sun, Inorg. Chem. 41, 455 (2002).
- [20] W. Farfán, E. Mosquera, R. Vadapoo, S. Krishnan, C. Marín, J. Nanosci. Nanotechnol. 10, 5847 (2010).
- [21] J. Wang, Z. Deng, Y. Li, Mater. Res. Bull. 37, 495 (2002).
- [22] W. Farfán, E. Mosquera, C. Marín, Adv. Sci. Lett. 4, 85 (2011).
- [23] T-Y. Ko, M. Shellaiah, K-W. Sun, Sci. Rep. 6, 35086 (2016).
- [24] K-W. Sun, T-Y. Fan, Mater. Sci. Appl. 1, 8 (2010).
- [25] RJ. Mehta, C. Karthik, W. Jiang, B. Singh, Y. Shi, RW. Siegel, T. Borca-Tasciuc, G. Ramanath, Nano Lett. 10, 4417 (2010).
- [26] J. Wei, L. Yang, Z. Ma, P. Song, M. Zhang, J. Ma, F. Yang, X. J. Wang, J. Mater. Sci. 55, 12642 (2020).
- [27] M. T. Pettes, J. Kim, W. Wu, K. C. Bustillo, L. Shi, APL Mater. 4, 104810 (2016).
- [28] S. Yazdani, M. T. Pettes, Nanotechnology 29, 432001 (2018).
- [29] B. Chakraborty, B. Ray, R. Bhattacharya, A. Dutta, J. Phys. Chem. Solids 4, 913 (1980).
- [30] H. R. Aliabad, F. A. Rad, Phys. B: Condens. Matter. 545, 275 (2018).
- [31] A. Jayaraman, A. Bhat Kademane, M. Molli, Indian J. Mater. Sci. 2016, ID7296847 (2016).
- [32] X. Wang, K. Cai, F. Shang, S. Chen, J. Nanopart. Res. 15, 1541 (2013).
- [33] X. Liu, X. Xiao, Y. Yang, D. J. Xue, D. B. Li, C. Chen, S. Lu, L. Gao, Y. He, M. Beard, Prog. Photovolt. Res. Appl. 25, 861 (2017).
- [34] T. Tritt, D. Rowe, *Thermoelectrics handbook: macro to nano* (CRC Press Boca Raton, FL; 2005).
- [35] H-S. Kim, Z. M. Gibbs, Y. Tang, H. Wang, G. J. Snyder, APL materials. 3, 041506 (2015).